

Unifying same- and different-material particle charging through stochastic scaling

Holger Grosshans,^{1,2,*} Gizem Ozler,^{1,2} and Simon Jantač¹

¹*Physikalisch-Technische Bundesanstalt (PTB), Braunschweig, Germany*

²*Otto von Guericke University of Magdeburg, Institute of Apparatus and Environmental Technology, Magdeburg, Germany*
(Dated: June 10, 2025)

Triboelectric charging of insulating particles through contact is critical in diverse physical and engineering processes, from dust storms and volcanic eruptions to industrial powder handling. However, repeated experiments revealed counterintuitive charge patterns, including variable impact charge under identical conditions, charge sign reversal with repeated impacts, and bipolar charging of differently sized particles. Existing computational models cannot predict these patterns; they either rely on oversimplified heuristics or require inaccessible detailed surface properties. We present a physics-based stochastic particle charging (SPC) model integrating experimentally characterized charging statistics into multiphase simulations. The model unifies same-material (particle-particle) and different-material (particle-wall) charging in a single framework, grounded in a stochastic closure by the mean, variance, skewness, and minimum impact charge of a single reference experiment. Implemented in a Lagrangian-Eulerian CFD solver, the SPC model takes less than 0.01% of the CPU time when simulating 300 000 insulating particles, charging during millions of same- and different-material contacts, transported by turbulent wall-bounded flows. By scaling the statistical parameters of the reference impact to each collision, the new model reproduces the complex charging patterns observed in experiments without requiring surface-level first-principles inputs. The SPC model offers a physically grounded route to massive-scale simulations of electrostatic effects across many fields of particle-laden flows.

I. INTRODUCTION

Contact charging of particles occurs in nature, such as in volcanic plumes [1], dust storms on Earth [2] and other planets [3], and in our lives, for example when grinding coffee [4]. In industrial powder processing, it can lead to wall fouling [5] and dust explosions [6].

Insulative particles are of particular concern due to their tendency to accumulate and retain high electrostatic charge. Earth's surface [7], coffee grinders [8], and industrial transport ducts are typically grounded and conductive, the latter to comply with safety regulations [9]. Despite the importance of charging insulative particles in turbulent flow along a conductive surface, there is currently no predictive, physically grounded charging model compatible with computational fluid dynamics (CFD) simulations.

A straightforward modeling approach would involve creating a large database of experimentally measured impact charges under various conditions. However, this strategy is infeasible in practice. For a single particle-surface combination, the impact charge depends on numerous variables, including temperature, humidity, pressure, impact mode, angle, velocity, particle size, shape, surface roughness, and initial charge. Building a statistically relevant dataset would require an impractically large number of experiments.

Even if such a dataset existed, experimental conditions often do not align with those in powder flows. For instance, the velocity-dependent charging model [10] re-

quired extrapolation to low impact velocities (<5 m/s) that were not accessible in the experimental setup.

The most widely used charging model in CFD is the condenser model, introduced more than five decades ago [11–13]. It is derived from electrostatics of conductive materials, where charge transfer is driven by the contact potential difference; thus, it applies to different-material charging.

The condenser model predicts that a particle repeatedly contacting another material charges until it saturates (Fig. 1a). The model computationally is fast and closed; its parameters, such as permittivity, surface resistivity, contact potential difference, and effective separation distance, can be measured experimentally. However, its application to systems involving insulative materials requires extensive parameter tuning and yields limited predictive power.

In particular, the condenser model fails to reproduce several experimentally observed patterns, out of which we highlight three we consider most important:

1. *Variable impact charge:* The condenser model is deterministic, predicting a fixed impact charge for given material properties and impact conditions. In contrast, different-material experiments with polymer particles show high variability even under carefully controlled conditions (Fig. 1b) [14, 17, 18].
2. *Charge reversal:* Under repeated contacts of different materials or asymmetric sliding, the direction of net charge transfer can reverse (Fig. 1c) [15, 19], an effect incompatible with the condenser model.
3. *Size-dependent bipolar charging:* Collisions between particles of the same material often result in particles of different sizes acquiring opposite charges (Fig. 1d) [16, 20], a phenomenon the condenser model

* Corresponding author; holger.grosshans@ptb.de

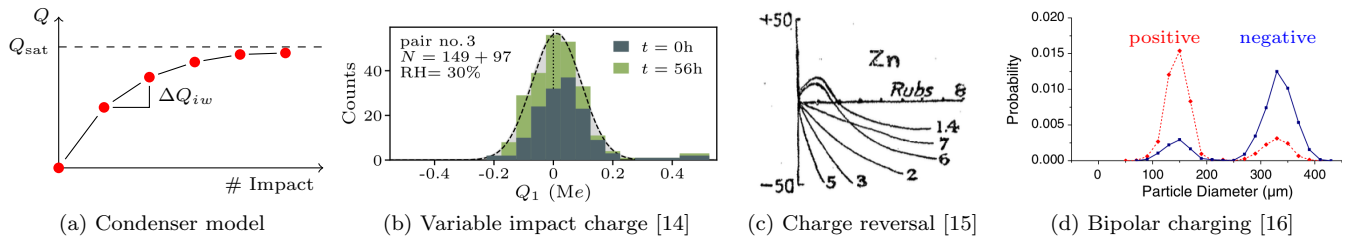


FIG. 1. (a) The classical condenser model predicts impact charge (ΔQ_{iw}) between materials strictly according to their contact potential difference, resulting in monotonic charging of a particle until it reaches its saturation charge (Q_{sat}). The model fails to reproduce several experimentally observed charging patterns: (b) stochastic variability in impact charge under identical conditions, (c) charge reversal, where the direction of net charge transfer between materials can invert after repeated contacts, and (d) size-dependent bipolar charging in contacts between particles of the same material but different sizes (adapted and reprinted with permission).

cannot predict due to its contact potential difference-driven directionality.

All these phenomena were explained in a somewhat similar way, by charging sites [14, 21], films [15], or charge carrier [22, 23], on the material surfaces that behave stochastic or change in time. Various extensions to the condenser model have been proposed to address specific shortcomings, such as charge scatter [24] or size-dependent effects [25], but none offers a general or robust solution.

The surface state model, as an alternative to the condenser model, focuses on charging between insulative materials with homogeneous surface composition [19, 22, 23, 26]. This model introduces the concept of a limited reservoir of transferable charge carriers on each particle's surface. As charge transfers, this reservoir depletes.

The surface state model can, contrary to the condenser model, predict size-dependent bipolar charging. For wall-bounded turbulent flow, this model showed that large particles charge positively and mid-sized ones negatively when colliding with other particles [27]. However, it applies only to contacts between insulators of the same materials, not to the critical case of particle-wall (insulator-conductor) contacts. Furthermore, the quantity of transferable charge carriers is generally unknown and treated as a tunable parameter.

At a more fundamental level, mosaic or patch models describe contact charging from first principles by resolving the contacting material's surfaces. On the resolved surface, they model charge transfer between nanoscopic donor and acceptor sites [28]. Charge transfer occurs probabilistically at these sites, resulting in a net stochastic outcome. This nanoscale mechanism has been qualitatively validated using Kelvin probe force microscopy (KPFM) [29–31].

Recent extensions of the mosaic model incorporate global differences in donor/acceptor densities [32], bridging the gap between same-material and different-material charging. Through this extension, the model captures all three charging patterns listed above. However, this model's practical use for large-scale particle systems is

limited by its dependence on inaccessible nanoscopic surface quantities, such as site correlation lengths and transfer probabilities. Moreover, applications remain confined to domains spanning a few micrometers.

To address these limitations, a scaling methodology has recently been developed to extend the mosaic model to full-scale powder flow simulations using discrete element modeling [33]. Yet even this approach applies only to same-material charging and requires unmeasured quantities.

In this work, we propose the stochastic particle charging (SPC) model that captures, inspired by the extension of the mosaic model by Grosjean and Waitukaitis [32], the stochastics of contact charging while remaining computationally efficient and compatible with CFD-scale simulations. The SPC model generalizes to particle-particle (insulator-insulator) and particle-wall (insulator-conductor) interactions. It treats impact charge as a random variable, whose statistical distribution, defined by its mean, standard deviation, and skewness, is derived from particle impact experiments under reference conditions. These distributions are then scaled based on local impact parameters to generate realistic charge outcomes throughout a simulated powder flow. The SPC model equation system is closed; it does not rely on any tuning through unmeasurable quantities.

In Section II, we derive the SPC model formulation. Section II G describes the experimental procedure to extract the statistical parameters of the reference impact required by the model. In Section III, we present large-scale CFD simulations that use the SPC model to predict the charging of PMMA and PS particles in turbulent flow bounded by an aluminum surface. Finally, we discuss the model's errors, predictive capabilities, and computational advantages.

II. STOCHASTIC PARTICLE CHARGING MODEL

A. Overview of the model concept

The particle charging model proposed here aims to predict the electrostatic charging of insulative particles as they contact either one another or conductive, grounded boundary walls. Figure 2 illustrates the underlying concept for both interaction types.

As shown in the schematic, we denote the charge transferred from the wall to particle i as $Q_{w \rightarrow i} = Q_w$, and the charge transferred from particle i to another contacting surface, either the wall or another particle j , as $Q_{i \rightarrow} = Q_i$. Based on this notation, the impact charge, i.e., the net charge change of particle i during wall contact (Fig. 2a) is

$$\Delta Q_{iw} = Q_w - Q_i, \quad (1a)$$

and during particle-particle contact (Fig. 2b), it is

$$\Delta Q_{ij} = Q_j - Q_i. \quad (1b)$$

According to the mosaic and surface state models, the contact area between a particle and another surface comprises charge-exchange sites that can be active, which means their charge carriers can transfer. In the generic formulation of the SPC model, the concepts of *active charging sites* and *transferable charge carriers* are equivalent, and we use the terms in this paper synonymously. Further, the SPC model makes no assumptions about these sites' spatial geometry or nanostructure.

The surface density of charging sites is c , and a ratio of α of them is active. In Fig. 2, black markers represent the active charging sites on the wall surface, green markers indicate active charging sites on the particle surfaces, and brown markers denote inactive charging sites.

Measurements of charge exchange between conductive particles and surfaces [17, 18] show that the variation of their impact charge is minuscule compared to the variation of the impact charge between insulators. Thus, we assume that charge transfer from the wall to the particle, Q_w , is deterministic. Each of N_w active charging sites on the wall contributes a charge ϵ_w to the particle, driven by a contact potential difference or any other physical mechanism. The model does not rely on a specific mechanism and thus remains broadly applicable. The total transferred charge from the wall is therefore

$$Q_w = \epsilon_w N_w \sim F(\mu_w), \quad (2a)$$

where μ_w is the expected value of Q_w . Because the wall is conductive and grounded, the charging sites refresh immediately after contact, maintaining a constant population of active sites before and after impact, as depicted in Fig. 2a.

In contrast, charge transfer from an insulative particle surface is assumed to be stochastic, in accordance with

the mosaic model [32]. The contact area of particle i includes N_i active charging sites, each of which can either transfer a charge ϵ_p to the opposing surface or not. This stochastic process follows a binomial distribution, which we approximate by a skewed normal distribution characterized by a mean μ_i , standard deviation σ_i , and skewness γ_i ,

$$Q_i = \epsilon_p \sum_{n=1}^{N_i} \theta_n \sim G(\mu_i, \sigma_i, \gamma_i), \quad (2b)$$

where θ_n is a Bernoulli random variable with equal probability of 0 or 1. Unlike the conductive wall, the insulative particle's active charging sites deplete during contact, reducing the number of active charging sites after impact, as shown by the reduced green markers in Figs. 2a and 2b.

We assume that ϵ_w and ϵ_p are constant for a given powder, an assumption that aligns with Grosjean and Waitukaitis [32]. Beyond this, the model does not require specification of the charge-exchange sites' size, shape, or nanoscopic structure. The parameters ϵ_w and ϵ_p represent quantized transferable charge carriers and are integer multiples of the elementary charge.

The polarities of ϵ_w and ϵ_p determine six distinct net charge distributions after impact (see Fig. 3). When ϵ_w and ϵ_p have opposite signs, the resulting distributions are strictly unipolar: either always negative (Type A2) or always positive (Type C1). If ϵ_w and ϵ_p have the same sign, the net impact charge can still be unipolar, provided the wall's contribution dominates (Types A1 and C2). However, if the particle's contribution is comparable, the distributions span both polarities, resulting in bipolar distributions (Types B1 and B2).

The charge histograms can identify the principal distribution types (A, B, or C). Distinguishing subtypes (1 or 2) requires further analysis. In our particle impact experiments, the charge distribution's tails extend into the negative domain. Given that electrons are the most probable charge carriers from grounded conductors suggests $\epsilon_w < 0$. If the distribution spans both signs, then $\epsilon_p < 0$ as well (i.e., Type B1). If the distribution is unipolar negative, the charge carriers are probably the same polarity but the wall contribution dominates; thus, Type A1 is most likely, but A2 cannot be entirely excluded. Therefore, Types A1 and B1 appear to be most representative of the materials examined in this study. Importantly, the model remains general in form and does not depend on the identity of the specific charge carriers.

B. Scaling the statistical parameters: $\mu_w, \mu_i, \sigma_i, \gamma_i$

As described in Section II G, particle impact experiments provide, for a defined reference condition (denoted by the subscript 0), the statistical parameters of the impact charge distribution. These parameters, shown in Fig. 4, serve as the basis for scaling the charge transfer distributions under varying impact conditions.



FIG. 2. (a) Particle and wall before (left), during (middle), and after contact (right). The white circles indicate the contact areas. Small dots are charge carriers on the surfaces' charging sites; their surface density is c . A ratio of α charging sites are active. Brown charging sites are inactive, and their charge carriers remain during contact on the surfaces. Black sites transfer charge carriers from the wall to the particle and are thus no longer available for subsequent transfer. As the wall is grounded and conductive, these sites instantly regenerate. On the particle, active charging sites (green) transfer charge carriers to the wall with a probability of p , reducing the particle's reservoir of transferable charge carriers. (b) The same mechanism applied to particle-particle contact. During impact, green charge carriers transfer between the two insulative particles, depleting the number of transferable carriers on both surfaces.

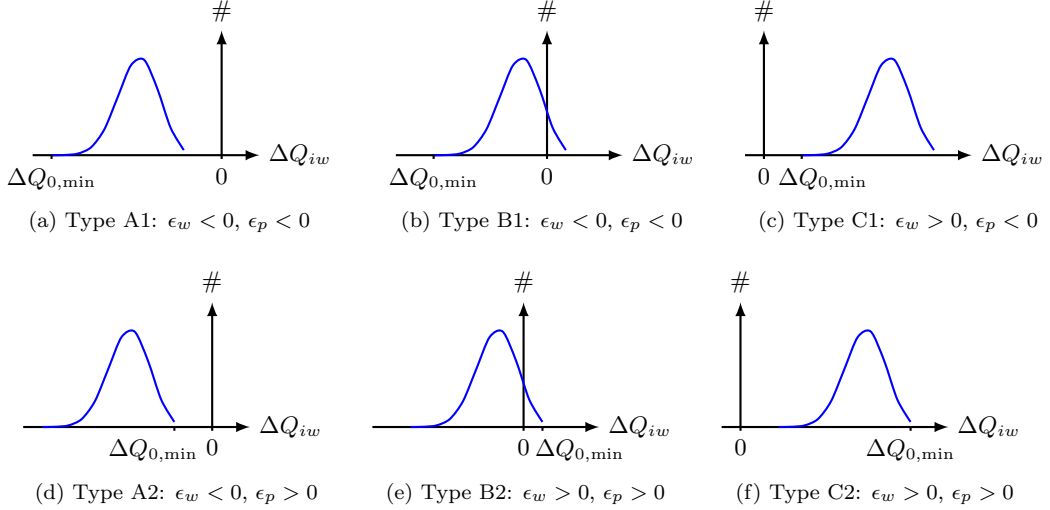


FIG. 3. Three possible impact charge distributions (Types A, B, and C) for contacts between fresh, uncharged, insulative particles and a conductive wall (sketched for negative skewness). Each distribution type allows two distinct interpretations (labeled 1 and 2) regarding the polarity of the transferred charge carriers ϵ_w from the wall and ϵ_p from the particle. Types A1 and B1 appear to be most representative of the materials in this study; nevertheless, the model is constructed in a general form.

According to Eq. (2a), a grounded conductive wall transfers the charge

$$\mu_w = \epsilon_w N_w \quad (3a)$$

to a particle. The charge transfer from an insulative particle follows, based on Eq. (2b), a binomial distribution, characterized by the mean

$$\mu_i = \epsilon_p N_i p, \quad (3b)$$

standard deviation

$$\sigma_i = \epsilon_p \sqrt{N_i p(1-p)}, \quad (3c)$$

and skewness

$$\gamma_i = \frac{1-2p}{\sqrt{N_i p(1-p)}}, \quad (3d)$$

where p is the probability that an active site transfers charge. Equations (3b) to (3d) hold analogously for particle j in a particle-particle contact.

The key challenge in solving Eqs. (3a) to (3d) lies in the nanoscopic parameters ϵ_w , ϵ_p , p , N_w , and N_i , which are not directly measurable. The SPC circumvents this challenge by scaling the parameters of the reference impact. For the reference impact, the same expressions become

$$\mu_{w0} = \epsilon_w N_{w0}, \quad (4a)$$

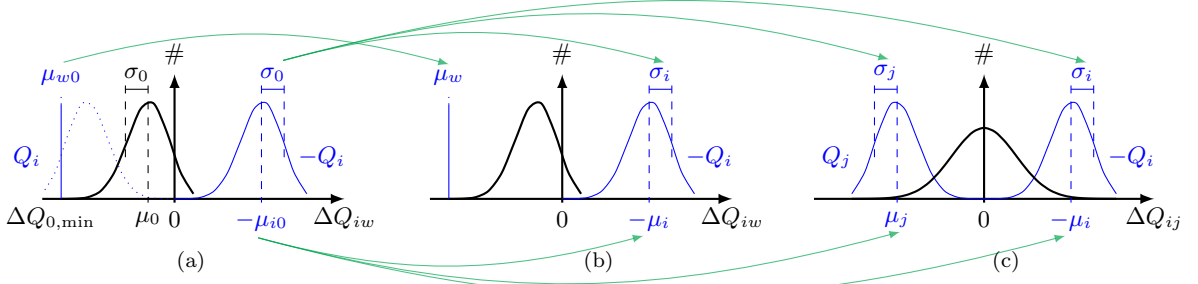


FIG. 4. (a) The impact charge distribution from particle impact experiments (black, Type B1) provides the statistical parameters μ_0 , σ_0 , γ_0 , and $\Delta Q_{0,\min}$. We decompose this distribution into the transfers (blue) from the wall and the particle. The SPC model scales these parameters (green arrows) to each contact: (b) For particle-wall contacts, to μ_w , μ_i , σ_i , and γ_i ; (c) For particle-particle contacts, to μ_i , σ_i , γ_i , μ_j , σ_j , and γ_j . (For clarity, skewness values γ_0 , γ_i , and γ_j are not shown in the plots.) Superimposing the contributions gives the impact charge distribution (black) per contact.

$$\mu_{i0} = \epsilon_p N_0 p, \quad (4b)$$

$$\sigma_{i0} = \sigma_0 = \epsilon_p \sqrt{N_0 p(1-p)}, \quad (4c)$$

$$\gamma_{i0} = -\gamma_0 = \frac{1-2p}{\sqrt{N_0 p(1-p)}}, \quad (4d)$$

where N_{w0} and N_0 represent the active charging sites for the wall and the particle, respectively, during the reference impact. Because all variation of the impact charge stems from the insulative particle, the standard deviation of the charge transfer from the particle equals the overall standard deviation of the impact charge (Eq. (4c)). The skewness changes sign (Eq. (4d)) because of the sign convention in Eq. (1a).

From these definitions, we derive the scaling laws for the particle-wall and particle-particle charge transfer parameters. Taking the ratio of Eq. (3a) to Eq. (4a) gives the scaled wall-to-particle mean charge transfer,

$$\mu_w = \mu_{w0} \frac{N_w}{N_{w0}}. \quad (5)$$

Likewise, the scaled mean of the particle-to-surface transfer follows from the ratio of Eq. (3b) to Eq. (4b),

$$\mu_i = \mu_{i0} \frac{N_i}{N_0}. \quad (6)$$

Besides the ratios of the charging sites (N_i/N_0 and N_w/N_{w0}), Eqs. (5) and (6) contain the unknowns μ_{w0} and μ_{i0} .

To resolve μ_{i0} , we use the mean of the charge balance Eq. (1a) for the reference impact, yielding

$$\mu_{i0} = \mu_{w0} - \mu_0. \quad (7)$$

This leaves the remaining unknown μ_{w0} , the mean wall-to-particle charge transfer in the reference condition.

We approximate μ_{w0} by the minimum observed impact charge in the reference experiment, $\Delta Q_{0,\min}$. This estimate assumes that the smallest recorded impact charge

corresponds to zero particle-to-wall charge transfer ($Q_i = 0$). This approximation is asymptotically valid in the limit of large experimental sample size,

$$\mu_{w0} = \lim_{M \rightarrow \infty} (\Delta Q_{0,\min}) \approx \Delta Q_{0,\min}. \quad (8)$$

Since the available experimental dataset may not fully reach this limit, we test the sensitivity of our simulations to this assumption in Section IV B.

Using the approximation of Eq. (8), we can finally express the scaled mean charge transfer from the wall to a particle as

$$\mu_w = \Delta Q_{0,\min} \frac{N_w}{N_{w0}} \quad (9a)$$

and from a particle to another surface as

$$\mu_i = (\Delta Q_{0,\min} - \mu_0) \frac{N_i}{N_0}. \quad (9b)$$

Further, the scaled standard deviation is obtained from Eq. (3c) and Eq. (4c),

$$\sigma_i = \sigma_0 \sqrt{\frac{N_i}{N_0}}, \quad (9c)$$

and the scaled skewness from Eq. (3d) and Eq. (4d) is

$$\gamma_i = -\gamma_0 \sqrt{\frac{N_0}{N_i}}. \quad (9d)$$

The scaling laws in Eqs. (9a) to (9d) define the statistical properties of particle-wall charge transfer. For particle-particle contacts, the corresponding parameters for both particles (i and j) follow Eqs. (9b) to (9d) and analogous expressions for j . The ratios N_i/N_0 and N_w/N_{w0} scale the contact-specific statistics from the reference condition and are further addressed in the next section.

The wall's charge transfer, Q_w , remains deterministic via Eq. (2a), while the particle's contribution, Q_i , follows a binomial distribution. For sufficiently large N_i , a binomial distribution is well-approximated by the skewed

normal distribution. Thus, Q_i is sampled from a skewed normal distribution defined by its statistical parameters, with the probability density function

$$g(Q_i; \mu_i, \sigma_i, \gamma_i) = \frac{1}{\sigma_i \sqrt{2\pi}} \exp\left(-\frac{(Q_i - \mu_i)^2}{2\sigma_i^2}\right) \cdot \left[1 + \operatorname{erf}\frac{\gamma_i(Q_i - \mu_i)}{\sqrt{2}\sigma_i}\right] \quad \text{for } 0 \leq Q_i \leq Q_{i,\max}. \quad (10)$$

. Since the skewed normal distribution is continuous, its tails extend to $\pm\infty$, while Q_i is physically limited by the finite number of active charging sites. The lower bound $Q_i = 0$ corresponds to no charge transfer; the upper bound $Q_{i,\max}$ corresponds to all active sites transferring charge. As shown in Appendix A, this upper limit is given by the closed-form expression

$$Q_{i,\max} = \frac{\mu_i (\gamma_i \mu_i - 2\sigma_i)}{\gamma_i \mu_i - \sigma_i}. \quad (11)$$

To ensure the total probability of the truncated distribution remains unity, we normalize Eq. (10). To generate stochastic realizations of Q_i , we apply an inversion sampling method using uniformly distributed pseudorandom numbers.

C. Active charging sites: N_i/N_0 and N_w/N_{w0}

The scaling relations (9a) to (9d) derived in the previous section require approximating the ratios N_i/N_0 and N_w/N_{w0} . A key advantage of the SPC model is that it relies only on these relative quantities, rather than requiring knowledge of the absolute number of charging sites.

If the particle and wall surfaces are homogeneous, the product of the contact area, A , and the surface density of active charging sites gives the number of active charging sites. At the wall, the charging sites regenerate instantaneously, so their surface density remains constant. In contrast, the initial surface density on the particle, c_0 , depletes over time due to charge transfer, so that $0 \leq c/c_0 \leq 1$.

Additionally, the local electric field around the particle can act as a force on the charge carriers against their path from one surface to the other. Then, the local electric field reduces the ratio α of active charging sites, such that $0 \leq \alpha/\alpha_0 \leq 1$, where α_0 is the ratio in the absence of a surrounding electric field.

Combining these effects, the number of active charging sites relative to the reference condition scales as

$$\frac{N_w}{N_{w0}} = \frac{A}{A_0} \frac{\alpha}{\alpha_0} \quad \text{and} \quad \frac{N_i}{N_0} = \frac{A}{A_0} \frac{\alpha}{\alpha_0} \frac{c}{c_0}. \quad (12)$$

The next sections develop physical approximations for the ratios A/A_0 (Section IID), α/α_0 (Section IIE), and c/c_0 (Section IIF).

D. Contact surface area: A/A_0

We model the ratio A/A_0 using Hertzian elastic contact theory and consider additionally the effect of surface roughness and the contact mode. For particle-wall interactions, i.e., a smooth spherical particle impacting a flat surface with the normal velocity $v_{n,i}$, the contact area A_w is [13]

$$A_w = \pi r_i^2 \left(\frac{5}{8} \pi \rho_p (1 + k_e) v_{n,i}^2 (\chi_p + \chi_w) \right)^{2/5}, \quad (13)$$

where k_e is the particle's restitution coefficient. The elasticity parameters of the wall, χ_w , and particle, χ_p , are given by $(1 - a^2)/b$, where a and b are their Poisson ratios and Young moduli, and usually $\chi_p \gg \chi_w$.

The ratio of the contact area to that of a reference impact becomes

$$\frac{A}{A_0} = \frac{A_w}{A_0} = \beta_c \left(\frac{r_i}{r_0} \right)^{2\beta_r} \left(\frac{v_{n,i}}{v_0} \right)^{4/5}, \quad (14)$$

where r_0 and v_0 are the reference particle radius and normal impact velocity. The coefficient β_c accounts for the effective increase in contact area due to rolling and sliding motion during wall contacts. For flows parallel to walls, such as in pneumatic transport systems, the tangential impact velocity can exceed the normal component by up to three orders of magnitude. Under such conditions, we assume that the particle rolls once over its circumference during contact and further increases the effective contact area due to sliding, leading to $\beta_c = 4\beta_a r_i (\pi/A_w)^{1/2}$ with $\beta_a = 1$. Only for simulations 1 and 2 (cf. Table II), β_a is larger than unity to shorten the computation duration.

The coefficient β_r accounts for the effect of surface roughness on the contact area. Note that β_r compensates for surface roughness in the ratio A_w/A_0 , which is a minor influence compared to the absolute influence of roughness on A_w . Based on our earlier findings [34], we adopt $\beta_r = 2.4$.

For particle-particle collisions, Hertz's theory provides the expression

$$A_{ij} = \frac{\pi r_i^2 r_j^2}{r_i + r_j} \left(\frac{5}{8} \pi \rho_p (1 + k_e) v_{ij}^2 \frac{\sqrt{r_i + r_j}}{r_i^3 + r_j^3} \chi_p \right)^{2/5} \quad (15)$$

for the contact area [11], where v_{ij} denotes the relative impact velocity of the colliding particles with radii r_i and r_j . Accordingly, the ratio to the reference contact area is

$$\frac{A}{A_0} = \frac{A_{ij}}{A_0} = \left(\frac{r_i^5 r_j^5}{r_0^5 (r_i + r_j)^2 (r_i^3 + r_j^3)} \frac{v_{ij}^2}{v_0^2} \frac{\chi_p}{\chi_p + \chi_w} \right)^{2\beta_r/5}. \quad (16)$$

Since $\chi_p \gg \chi_w$, the above simplifies to

$$\frac{A}{A_0} = \frac{A_{ij}}{A_0} = \left(\frac{r_i^5 r_j^5}{r_0^5 (r_i + r_j)^2 (r_i^3 + r_j^3)} \frac{v_{ij}^2}{v_0^2} \right)^{2\beta_r/5}. \quad (17)$$

In summary, Eqs. (14) and (17) provide the scaling laws for the contact area used in Eq. (12). The present model is based on classical Hertzian theory and additionally accounts for surface roughness and contact mode. It can be systematically extended to include more complex contact mechanics, for example, of non-spherical particles or varying contact modes [35, 36], all of which can be incorporated into the scaling ratio A/A_0 .

Overall, comparing Eq. (14) and Eq. (17) to Eq. (13) and Eq. (15) demonstrates once more the advantage of the SPC model building throughout on ratios instead of absolute quantities, which cancels out most material-dependent parameters.

E. Activity ratio: α/α_0

In the reference experiment, particles are initially uncharged before impact and shielded from external electric fields. As a particle accumulates charge, the surrounding electric field E increases, hindering charge transfer in subsequent collisions. This suppression of charge transfer is captured by the ratio of active charging sites, α , generally expressed as [33]

$$\alpha = \alpha_0 \left(1 - \text{sgn}(\epsilon) \frac{E}{|E_{\text{sat}}|} \right) \quad \text{with} \quad 0 \leq \alpha \leq \alpha_0 \quad (18)$$

where α_0 is the ratio of a particle without an electric field, and E_{sat} is the saturation field strength at which all sites cease to transfer charge. The sign function accounts for the directionality of the field with respect to the charge carrier's polarity.

For the specific transferable charge carrier, the sign function is expressed in quantities of the reference impact by $\text{sgn}(\epsilon_p) = \text{sgn}(\Delta Q_{0,\text{min}} - \mu_0)$ and $\text{sgn}(\epsilon_w) = \text{sgn}(\Delta Q_{0,\text{min}})$. Then, the above relation leads to the normalized form for the ratio of active sites at a wall,

$$\frac{\alpha}{\alpha_0} = \frac{\alpha_w}{\alpha_0} = 1 + \text{sgn}(\Delta Q_{0,\text{min}}) \frac{E_i}{|E_{\text{sat}}|}, \quad (19a)$$

a particle contacting a wall,

$$\frac{\alpha}{\alpha_0} = \frac{\alpha_i}{\alpha_0} = 1 - \text{sgn}(\Delta Q_{0,\text{min}} - \mu_0) \frac{E_i}{|E_{\text{sat}}|}, \quad (19b)$$

and a particle contacting another particle,

$$\frac{\alpha}{\alpha_0} = \frac{\alpha_{ij}}{\alpha_0} = 1 - \text{sgn}(\Delta Q_{0,\text{min}} - \mu_0) \frac{E_{ij}}{|E_{\text{sat}}|}, \quad (19c)$$

with $0 \leq \alpha/\alpha_0 \leq 1$.

The field strength E_i at the surface of a charged particle during contact with a conductive wall is

$$E_i = -\frac{1}{2\pi\epsilon} \frac{Q_i}{r_i^2}, \quad (20a)$$

and during contact with another particle

$$E_{ij} = \frac{1}{4\pi\epsilon} \left(\frac{Q_j}{r_j^2} - \frac{Q_i}{r_i^2} \right). \quad (20b)$$

The magnitude of the saturation field strength

$$|E_{\text{sat}}| = \frac{1}{2\pi\epsilon} \frac{|Q_{\text{sat}}|}{r_0^2}, \quad (21)$$

depends on the corresponding magnitude of the particle saturation charge, which we approximate by

$$|Q_{\text{sat}}| = C_{\text{sat}} r_0^2. \quad (22)$$

Here, $C_{\text{sat}} = 500 \mu\text{C m}^{-2}$ is a fitting parameter based on numerical simulations for air at atmospheric pressure and unit permittivity [17], which also aligns with experimental data [37]. Substituting Eq. (22) into Eq. (21) yields

$$|E_{\text{sat}}| = \frac{C_{\text{sat}}}{2\pi\epsilon}. \quad (23)$$

Using Eqs. (20a), (20b) and (23) in the expressions for α/α_0 , we obtain the final scaling relations for the active site ratio used in Eq. (12),

$$\frac{\alpha}{\alpha_0} = \frac{\alpha_w}{\alpha_0} = 1 - \text{sgn}(\Delta Q_{0,\text{min}}) \frac{Q_i}{C_{\text{sat}} r_i^2} \quad (24a)$$

$$\frac{\alpha}{\alpha_0} = \frac{\alpha_i}{\alpha_0} = 1 + \text{sgn}(\Delta Q_{0,\text{min}} - \mu_0) \frac{Q_i}{C_{\text{sat}} r_i^2} \quad (24b)$$

$$\frac{\alpha}{\alpha_0} = \frac{\alpha_{ij}}{\alpha_0} = 1 - \text{sgn}(\Delta Q_{0,\text{min}} - \mu_0) \frac{2}{C_{\text{sat}}} \left(\frac{Q_j}{r_j^2} - \frac{Q_i}{r_i^2} \right) \quad (24c)$$

with $0 \leq \alpha/\alpha_0 \leq 1$.

F. Charging site density: c/c_0

A particle undergoes M contacts with other surfaces, which occur at the time of t_M . Before the first contact ($t < t_1$), the surface density of charging sites remains unchanged from its initial value, c_0 , which equals the density on the surface of the levitated particle in the reference experiment. During the m th collision, the density reduces from c_{m-1} to c_m and the relative density reduces according to

$$\Delta \left(\frac{c}{c_0} \right)_m = \left(\frac{c_m - c_{m-1}}{c_0} \right) = -\frac{c_{m-1}}{c_0} \frac{A_m}{A_p} \frac{\alpha_m}{\alpha_0} \frac{Q_{i,m}}{Q_{i,\text{max}}}. \quad (25)$$

In this expression, the first term on the right-hand side represents the active charging site density on the surface before the m th impact. The second term, A_m/A_p , denotes the ratio of the contact area to the total particle

surface area, $A_p = 4\pi r^2$. The third and fourth terms capture the fraction of charge carriers transferred relative to those available in the contact region.

Summing up Eq. (25) over $M - 1$ impacts gives the charging site ratio between t_{M-1} and t_M ,

$$\begin{aligned} \frac{c}{c_0}(t_{M-1} < t \leq t_M) &= 1 - \sum_{m=1}^{M-1} \frac{c_{m-1}}{c_0} \frac{A_m}{A_p} \frac{\alpha_m}{\alpha_0} \frac{Q_{i,m}}{Q_{i,\max}} \\ &+ \sum_{m=1}^M \left(1 - \frac{c_{m-1}}{c_0}\right) \frac{t_m - t_{m-1}}{\tau_r}, \end{aligned} \quad (26)$$

with $0 \leq c/c_0 \leq 1$. The first summation accounts for depletion over successive impacts, as described by Eq. (25). The second term models the slow regeneration of charging sites, which occurs on a characteristic timescale τ_r . For insulative particles, the timescale τ_r is typically much larger than the time between contacts. Thus, regeneration of charge carriers can be neglected, and Eq. (26) simplifies to

$$\frac{c}{c_0}(t_{M-1} < t \leq t_M) = 1 - \sum_{m=1}^{M-1} \frac{c_{m-1}}{c_0} \frac{A_m}{A_p} \frac{\alpha_m}{\alpha_0} \frac{Q_{i,m}}{Q_{i,\max}}. \quad (27)$$

with $0 \leq c/c_0 \leq 1$.

Assuming $k_e = 1$ and $\chi_p \gg \chi_w$, the contact area ratio A_m/A_p becomes, for particle-wall impacts,

$$\frac{A_m}{A_p} = \frac{A_w}{A_p} = \beta_c \left(\frac{5}{128} \pi \rho_p v_{n,i}^2 \chi_p \right)^{2/5}, \quad (28a)$$

and for particle-particle interactions,

$$\frac{A_m}{A_p} = \frac{A_{ij}}{A_p} = \left(\frac{5}{128} \pi \rho_p v_{n,i}^2 \frac{r_j^5}{(r_i + r_j)^2 (r_i^3 + r_j^3)} \chi_p \right)^{2/5}. \quad (28b)$$

Substituting Eqs. (28a) and (28b) into Eq. (27) provides the depletion of the charging site density necessary for evaluating Eq. (12).

G. Reference impact: μ_0 , σ_0 , γ_0 , $\Delta Q_{0,\min}$

The SPC model derived in this section requires four input parameters (Fig. 4) for a defined reference impact: μ_0 , σ_0 , γ_0 , and $\Delta Q_{0,\min}$. For the skewness, we found it more accurate to use the alternative expression Eq. (A4) with $p = (\mu_0 - \Delta Q_{0,\min}) / (\Delta Q_{0,\max} - \Delta Q_{0,\min})$ and with $\Delta Q_{0,\max}$ being the maximal impact charge of the reference impact. As shown in Appendix A, this expression is equivalent to the skew of the raw data for converged statistical distributions.

To provide accurate and material-specific input data, we developed an apparatus to measure these quantities. This experiment enables precise control over initial and

TABLE I. Reference impact experiments.

Particle	PS	PS	PMMA
Target	aluminum	aluminum	aluminum
r (μm)	538	713	200
v_n (m/s)	1.1	1.1	0.9
Impacts	241	317	100
μ_0 (fC)	-68.5	-306.6	-4.1
σ_0 (fC)	72.3	183.5	6.5
γ_0 (-)	-0.56	-0.45	-0.19
$\Delta Q_{0,\min}$ (fC)	-462.0	-1842.0	-21.9

boundary conditions, minimizing scattering in the results. The setup, sketched in Fig. 5, achieves a measurement uncertainty of less than 1 fC for the impact charge of a single particle.

The apparatus integrates and extends two established techniques, the experimental setup by Matsuyama *et al.* [17] and acoustic levitation. In comparable facilities, scattering often arises from unknown initial charge distributions on the particle surface. To mitigate this uncertainty, particles are initially levitated in an acoustic trap. This contact-free handling prevents unwanted triboelectric charging and allows the neutralization of surface charges using an ionization needle. Additionally, acoustic streaming clears ions from the vicinity of the particle, further reducing the unintended charge. Upon deactivating the levitator, the particle falls freely through a hole in the reflector towards the target.

All measurements were conducted in a climate-controlled chamber, where ambient temperature and relative humidity were maintained at 25 °C and 10%, respectively. The drop height of 10 cm to 15 cm allows particles of $r = 200 \mu\text{m}$ to reach normal impact velocities of approximately 1 m/s due to gravity. This velocity range is representative of typical wall-normal impact velocities in flows parallel to walls, which are generally below 10% of the streamwise gas velocity.

The particle then enters a Faraday cage, impacts a conductive target (15 mm \times 15 mm, $\vartheta = 35^\circ$), and exits the cage. A high-speed CMOS camera with an integrated light source observes the target through a small optical window. These images are used to determine the particle's impact velocity. A digital oscilloscope, sampling at 25 μs to 500 μs intervals, records the initial and final charge of the particle.

The reference impact conditions and measured statistical parameters are listed in Table I. Experimental charge distributions and model fits are shown in Figs. 5b and 5c. This study demonstrates the SPC model for two powders, polystyrene (PS) and polymethyl methacrylate (PMMA), interacting with an aluminum wall.

For each material pair, the model requires only a single reference condition. Nonetheless, we conducted two reference experiments for PS to evaluate the accuracy of the model's scaling. These cases differ solely in particle size. As shown in Fig. 5b, the SPC model successfully predicts

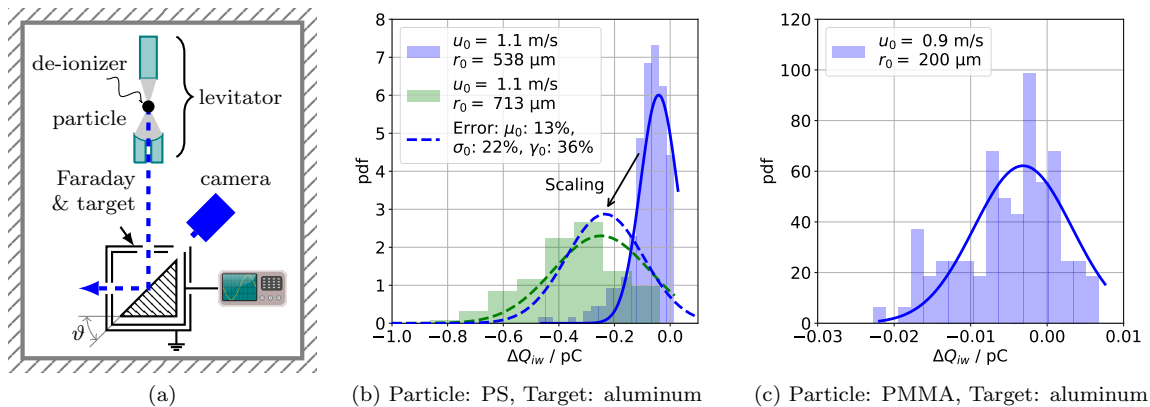


FIG. 5. (a) Schematic of the particle impact charging apparatus (not to scale). For each reference impact condition, ≥ 100 fresh, uncharged particles impact the target under identical conditions. (b) Reference impact results for polystyrene (PS) particles. Histograms display the raw measured charge distributions for two particle sizes. According to the SPC model, the distribution of the larger particles is predicted by scaling the statistical parameters obtained from the smaller particles. (c) Reference impact results for poly(methyl methacrylate) (PMMA) particles.

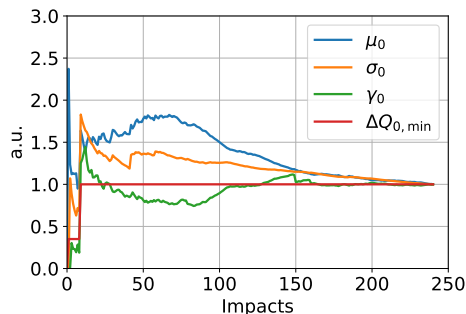


FIG. 6. Convergence of the statistical parameters of the reference impact of PS particles with $r = 538$ μm . Each parameter is plotted relative to its final value after 241 impacts.

the impact statistics of the larger particles based on the smaller-particle reference, with errors between 13% and 36%.

These deviations stem from several sources, one being the statistical error due to a finite number of measurements. For a normally distributed sample, the standard error of the skewness ($\approx (M/6)^{-1/2}$) drops the slower with the number of observations, M , compared to the standard errors of the mean ($= M^{-1/2}$) and standard deviation ($\approx (2M)^{-1/2}$). The error in $\Delta Q_{0,min}$ is binary; either the dataset captures the minimal impact charge or not, where the probability of capturing the minimal impact charge is $1 - (1 - (1 - p)^{N_0})^M$. Thus, the statistical uncertainties associated with γ_0 and $\Delta Q_{0,min}$ are the most difficult to constrain.

Figure 6 plots the sensitivity of the statistical parameters with the number of impacts for $r = 538$ μm sized PS particles. According to the figure, the statistical errors drop below 20% after 150 impacts.

After having established the statistical parameter's scaling accuracy (Fig. 5) and convergence (Fig. 6), we investigate the sensitivity of the model to these parameters in Section IV B.

H. Summary of the SPC model

To restate for clarity, the key relations of the model are Eqs. (9a) to (9d) and (12). These relations scale the statistical parameters of charge transfer from an experimentally well-characterized reference impact to a wide range of particle-wall and particle-particle contact conditions occurring in powder flows. The formulation is intentionally neutral regarding the physiochemical mechanisms of charge exchange, focusing instead on predicting stochastic charge distributions.

To illustrate the model's behavior, Fig. 7 shows representative results for generic input parameters (Type B1). These plots enable a qualitative discussion of the model response, while Section III provides quantitative results for specific conditions.

Figure 7a depicts statistical distributions of impact charge for uncharged particles ($\alpha_i/\alpha_0 = \alpha_w/\alpha_0 = 1$), with decreasing charging site density on the particle surface. As c/c_0 decreases, the distributions narrow, and their means shift leftward. For high c/c_0 , the distribution exhibits a tail extending into the positive domain. As the charging sites deplete ($c/c_0 < 0.75$ in this example), the impact charge becomes always negative. The sign of the impact charge reflects the relative magnitude of charge transfer: it is positive when the particle-to-wall transfer dominates and negative when the wall-to-particle transfer is larger. In the limit $c/c_0 \rightarrow 0$, all charging sites on the particle are depleted, and the impact charge converges to a deterministic value determined solely by the

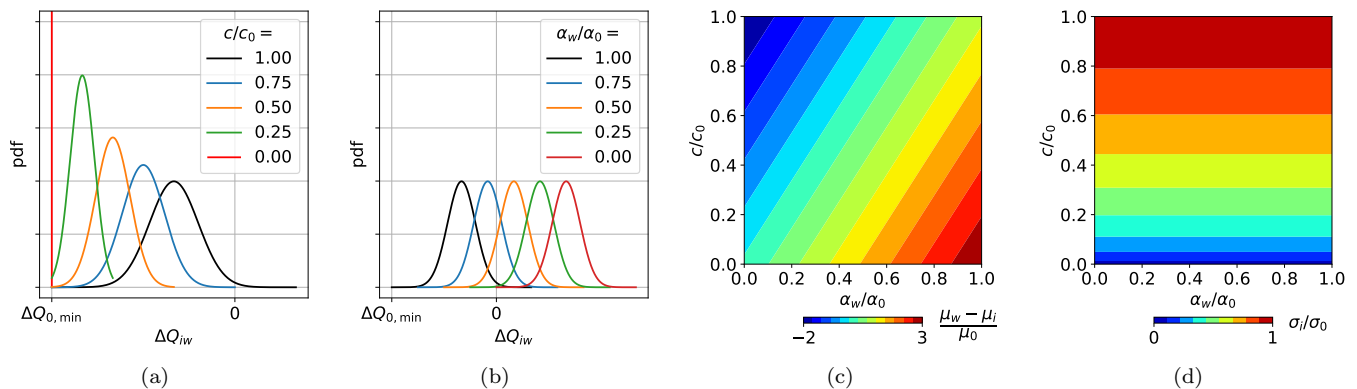


FIG. 7. Statistical parameters of repeated particle-wall impacts predicted by the SPC model for a constant contact area ($A/A_0 = \text{const}$, $\gamma_0 = 0$, Type B1; see Fig. 3). (a) Probability distributions of the impact charge for uncharged particles ($\alpha_w/\alpha_0 = 1$) with depleting charging sites on the surface. (b) Distributions for particles maintaining their initial charging site density ($c/c_0 = 1$) while their charge increases. (c) Mean and (d) standard deviation of the impact charge as functions of α_w/α_0 and c/c_0 .

wall's contribution. Then, the distribution collapses into a vertical line.

Figure 7b shows impact charge distributions for particles with constant $c/c_0 = 1$ and $\alpha_i/\alpha_0 = 1$, but decreasing α_w/α_0 , representing increasing particle charge. As α_w/α_0 decreases, the peaks of the distributions shift to the right because the charge transfer from the wall reduces. But the charge transfer from the particle to the wall is unaffected by α_w/α_0 , thus, the widths of the distributions remain constant. Unlike in Fig. 7a, the distributions remain bipolar until α_w/α_0 asymptotically approaches zero. At saturation, the electric field prevents further net charge transfer from the wall to the particle, and the impact charge is always positive.

Figures 7c and 7d present the evolution of the mean and standard deviation of the impact charge as functions of α_w/α_0 and c/c_0 . Particles traverse these surfaces over time, moving from the upper right corners (uncharged, carrier-rich) to the lower left corners (saturation-charged, carrier-depleted). Although the initial and final states may be identical, the path depends on the particle's impact history.

III. CFD SIMULATIONS

To assess whether the proposed model can predict *variable impact charge*, *charge reversal*, and *size-dependent bipolar charging*, we conducted simulations with thousands of PS and PMMA particles. The particles were released in generic geometries and flow conditions, specifically wall-bounded turbulent flows and periodic cubic boxes. Consistent with the reference impact measurements (Section II G), all walls in the simulations are composed of aluminum. Table II provides an overview of the parameters of all simulations.

We implemented the SPC model (Section II) into the open-source CFD tool pafix [38]. The code employs a coupled Eulerian-Lagrangian scheme in which particle-particle collisions are modeled using a hard-sphere approach. The gas-phase flow is resolved by Direct Numerical Simulation (DNS) of the incompressible Navier-Stokes equations, capturing all turbulent scales.

Individual particles are tracked in a Lagrangian reference frame, and their trajectories are computed by solving Newton's second law, accounting for drag, lift, electrostatic, gravitational, and collisional forces. A hybrid approach [39] computes electrostatic interactions, combining near-field Coulomb forces between neighboring particles with far-field forces obtained from Gauss's law. Collisional forces account for particle-particle and particle-wall interactions. Further details on the solver setup, numerical methods, and validation are given in Appendix B.

To evaluate *variable impact charge* and *charge reversal*, we simulated 300 000 particles in a wall-bounded turbulent flow (simulations 1–4; Table II). The domain geometry corresponds to a downward-oriented square duct with a side length of 5 cm. We simulate a duct section with periodic boundary conditions in the streamwise direction, driving the flow by a constant pressure gradient and gravitational acceleration. Based on the duct width, the flow has a bulk Reynolds number of approximately 5400 and a friction Reynolds number of 360. Each simulation begins with electrostatics disabled to allow the gas and particle flow to reach a statistically stationary state. Once the flow is fully developed, the SPC model is activated.

To assess *size-dependent bipolar charging*, we simulated 62 500 particles in a cubic domain of side length 5 cm (simulations 5 and 6; Table II). To isolate the effect of particle-particle collisions, we employed periodic boundary conditions on all sides, thereby eliminating wall con-

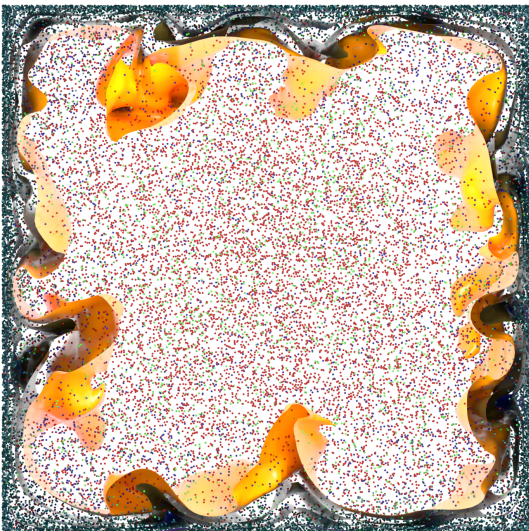


FIG. 8. Snapshot of 200 μm sized PMMA particles in a wall-bounded turbulent flow (simulation 2; Table II). The snapshot depicts the cross-section and 10% of the domain in the downstream direction at the time instance when $\overline{c/c_0} = 0.5$. The isosurfaces visualize constant streamwise velocity magnitude of the gas. Cyan particles contacted a wall, and green particles contacted another particle within the last millisecond. Particles that did not collide recently are colored by their polarity: red indicates positive, blue negative charge.

tacts. Further, only collisional and electrostatic forces act on the particles; fluid forces (drag and lift) and gravity are omitted. Particles are initialized at random positions with velocities of 5 m/s in random directions.

Particles are either PS, with a density of $\rho_p = 1000 \text{ kg m}^{-3}$, or PMMA, with a density of $\rho_p = 1150 \text{ kg m}^{-3}$. Due to their similar elastic properties, both materials are assigned the same elasticity parameter, $\chi_p = 2.9 \times 10^{-10} \text{ s}^2 \text{ m kg}^{-1}$ [40, 41]. The aluminum walls are modeled with an elasticity parameter of $\chi_w = 1.25 \times 10^{-11} \text{ s}^2 \text{ m kg}^{-1}$ [41]. In all simulations, the coefficient of restitution is unity. We report results for both monodisperse systems (with particle diameters of 100 μm or 200 μm) and bidisperse mixtures containing both sizes.

Figure 8 shows a snapshot from simulation 1 (Table II) of 300 000 PMMA particles (monodisperse, $r = 200 \mu\text{m}$) in a wall-bounded turbulent flow. The figure shows 10% of the total flow domain and particle number. The isosurfaces of the streamwise velocity (0.38 m/s, 0.75 m/s, 1.13 m/s, and 1.50 m/s) visualize the complex fluid structures. The particles are colored by their instantaneous net charge or collision history. Particles that have collided with a wall within the last millisecond are rendered in cyan, whereas those that recently underwent a particle-particle collision appear in green. This visualization highlights the dynamic interplay between turbulent transport and collisional charging.

As particles interact with walls and each other, their charge evolves in time according to the SPC model. In the depicted case, 300 000 particles collide on average 1.5 million times per second with a wall and 1.8 million times per second with each other. Despite its particle-wise application at each collision, the SPC model remains computationally efficient, accounting for less than 0.01% of the total simulation runtime. This efficiency enables massive-scale simulations with fully resolved charge evolution at the particle scale, even in turbulent flow.

Figure 9a shows the temporal evolution of the average particle charge and the charging site density for 200 μm PS and PMMA particles (simulations 1 and 2; Table II). PMMA charges faster than PS. In both cases, the charging sites fully deplete over time, and the particles reach their saturation charges. For PMMA, the evolution of the normalized charge closely follows the depletion of the charging sites. In contrast, for PS, the increase in particle charge lags behind the depletion of charging sites. This delay arises because, for PS, the contribution of particle-to-wall charge transfer dominates, which reduces the net charging effectiveness as charging sites deplete. Consequently, although PS particles lose their charging sites, they initially accumulate less charge. Only after some amount of charging sites has been depleted, after about 6 s, does the net impact charge increase significantly, and PS charges at a rate comparable to that of PMMA.

Figures 9b and 9c present the corresponding charge distributions of the 200 μm PS and PMMA particles at selected time instances. For both materials, the SPC model captures the transition of the distributions from centering around uncharged particles toward peaking near the saturation charge. For PS, the relatively strong and stochastic particle-to-wall charge transfer results in a smooth progression of the distribution from being neutral to negatively charged.

The particle charge distributions approximate logarithmic functions at early and late times in the simulations. In Fig. 9c, the blue dotted curve illustrates the close agreement of the PMMA charge distribution at the final time instance with a logarithmic function of positive slope. After about $t = 2 \text{ s}$, the left tails of the distributions are logarithmic with a negative slope. Thus, a mixture of particles at different stages in their charging history, some having undergone few and some many collisions, would produce charge distributions with two exponential tails. This behavior demonstrates the SPC model's ability to reproduce non-Gaussian charge distributions as observed experimentally [42, 43].

Having established the general features of the charging dynamics, we now examine the three charging patterns highlighted in the Introduction.

A. Variable impact charge

We first demonstrate by Fig. 10 that the SPC model predicts *variable impact charge*, consistent with experi-

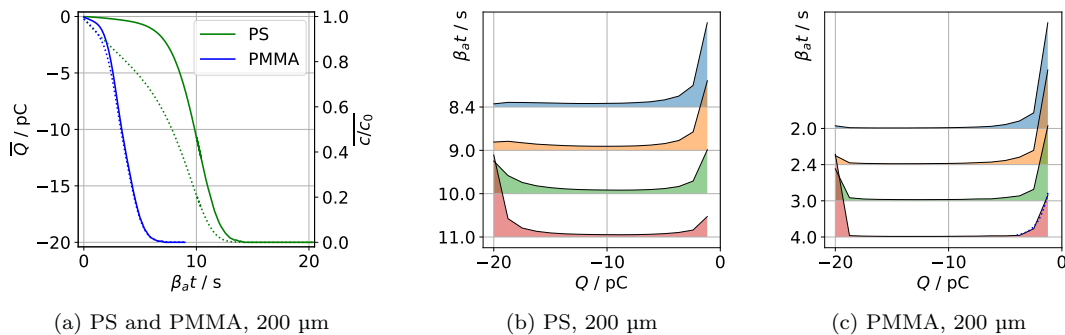


FIG. 9. (a) Temporal evolution of the particle charge and charging site density for 200 μm PS and PMMA particles transported in wall-bounded turbulent flow. (b) Charge distribution of PS particles at selected time instances. (c) Charge distribution of PMMA particles at selected time instances. The blue dotted line in (c) indicates a logarithmic fit to the distribution at 4.0 s.

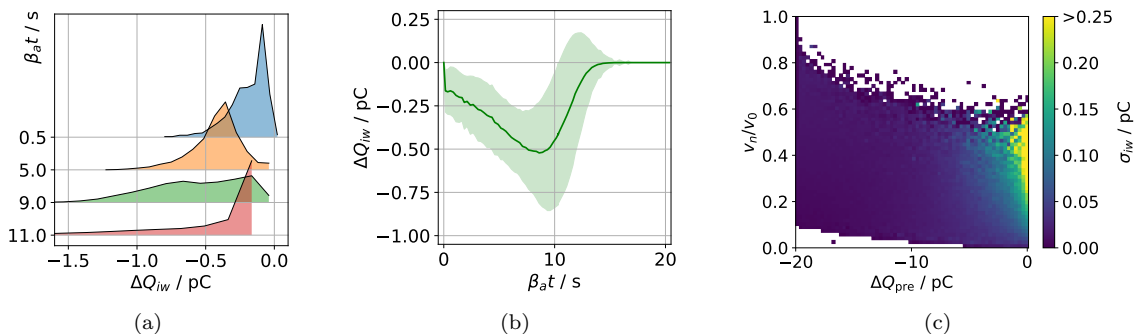


FIG. 10. (a) Variable impact charge of 200 μm sized PS particles predicted by the SPC model at selected time instances, consistent with experimental observations (cf. Fig. 1b). (b) Temporal evolution of the mean and standard deviation of the impact charge reflects changing impact conditions and particle properties over the course of the simulation. (c) For constant impact velocity and initial charge, the variation in impact charge arises from the stochastic particle-to-surface charge transfer as described by Eq. (10).

mental observations (Fig. 1b). Particles acquire different amounts of charge upon contact with a surface, even under nominally identical impact conditions. As evident from Eq. (10), this variability arises from the stochastic charge transfer from the insulating particle to another surface. The model thus inherently captures the experimentally observed spread in impact charge.

For wall-bounded turbulent flow, Fig. 10a shows the distributions of impact charge for 200 μm PS particles during wall collisions at selected time instances (simulation 1; cf. Table II). These distributions evolve over time, reflecting changes in the overall impact charge statistics driven by the depletion of charging sites and increasing particle charge. As shown in Fig. 10b, the initial impact charges are low due to the near balance between particle-to-wall and wall-to-particle charge transfer.

Until $t = 9$ s, the magnitude of the impact charge increases because the charging sites deplete, and wall-to-particle transfer dominates more and more. During this time, the impact charge distributions in Fig. 10a move toward the left. After approximately 9 s, the increasing

particle charge reduces the net impact charge due to electrostatic inhibition of further transfer. At $t = 14$ s, particles approach saturation, and the mean impact charge and its standard deviation tend toward zero.

However, even for identical initial charge and impact velocity, the impact charge remains variable, as shown in Fig. 10c. The variation of the impact charge is the highest for initially uncharged particles at high impact velocities, where the number of active charging sites, i.e., N_i/N_0 in Eq. (12), is large.

The SPC model, therefore, reproduces the variable impact charge observed in experiments [14, 17, 18]. This behavior supports the hypothesis that the variability arises from the stochastic charge transfer at individual contact sites on insulating surfaces.

The impact charge variability of PMMA particles (simulation 2; cf. Table II) is comparable to that of PS particles, as discussed in Appendix C.

B. Charge reversal

Second, we demonstrate *charge reversal* by analyzing the evolution of particle polarity during successive impacts, as shown in Fig. 11. To this end, we plot the charge histories of selected 100 μm sized PS and PMMA particles in wall-bounded turbulent flow (simulations 3 and 4; cf. Table II). Because there is no inherent directionality in same-material charge transfer, particles can undergo both positive and negative charge transfers during collisions with other particles. We neglect particle-particle charging in the simulations shown in Fig. 11 to isolate charge reversal at wall contacts with a different material.

As illustrated, the SPC model predicts charge reversal for some particles and not for others, qualitatively consistent with experimental observations (Fig. 1c). In agreement with those experiments, the polarity typically switches from positive to negative after the first or second wall contact. This outcome corresponds to the hypothesized mechanism underlying charge reversal: During the first impact, the particle surface contains a full layer of active charging sites. Depleting this layer can result in a net positive charge transfer from the wall to the particle. As collisions continue, the active charging sites on the particle surface deplete. The charging sites mostly being depleted shifts the charge transfer balance so that charge transfer from the wall to the particle dominates subsequent impacts, producing a net negative impact charge.

In wall-bounded turbulent flow, approximately one in four of the 100 μm PMMA particles initially charge positively, compared to only one in one eighty PS particles. These probabilities differ from those in the reference impact statistics (Fig. 5). This difference is because the charge transfer from the wall to the particle, μ_w , scales with the ratio of active charging sites, which, during the

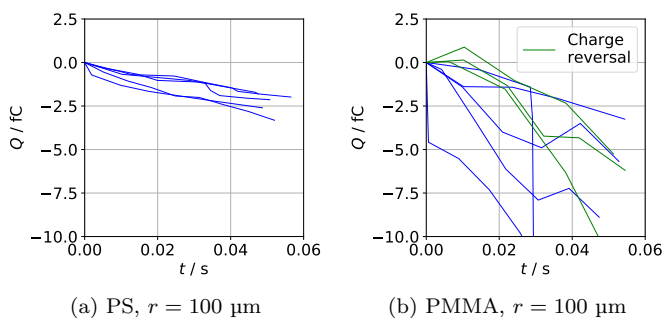


FIG. 11. Charge reversal during wall contacts of selected particles, as predicted by the SPC model and observed in experiments (Fig. 1c). Blue curves represent particles that charge negatively throughout the simulation. Green curves show particles that undergo charge reversal, first charging positive and then negative, consistent with experimental findings [15, 19]. The probability of initially acquiring a positive charge is twenty times higher for PMMA particles than for PS particles.

first impact, is proportional to the contact area ratio (cf. Eq. (3a)). Similarly, the mean charge transfer from the particle to the wall, μ_i , scales with the same ratio (cf. Eq. (3b)). However, the standard deviation of the transfer, σ_i , scales with the square root of the contact area (cf. Eq. (3c)). Since σ_i determines the likelihood that the particle-to-wall transfer exceeds the reverse, the probability of charge reversal is higher for particles with smaller contact areas. This explains why charge reversal is more prevalent in the 100 μm particles than in the 200 μm particles.

Importantly, the SPC model predicts charge reversal solely based on the scaling laws and the stochastic charge transfer statistics of the reference impact. The model contains no explicit switching mechanism.

C. Size-dependent bipolar charging

Third, Fig. 12 shows the capability of the SPC model to predict *size-dependent bipolar charging*. For this investigation, we consider only charge transfer between particles and do not account for charge transfer between particles and walls. Thus, we entirely omit the effect of walls and wall-bounded turbulence. Instead, the particles are released in a cubical box of 5 cm side length with an initial velocity of 5 m/s (simulations 5 and 6; cf. Table II).

For both particle materials, PS and PMMA, the distributions in Fig. 12 show size-dependent bipolar charging. The underlying mechanism is asymmetric charging, that is, different depletion rates of c/c_0 on the surfaces of smaller and larger particles. The active charging sites on the smaller particles deplete more quickly. Thus, starting from the second contact, the average net charge tends to transfer from the larger to the smaller particles.

In our case with charging Types A1 and B1 (Fig. 3), i.e., $\epsilon_p < 0$, this results in a net negative charge transfer from the larger to the smaller particles. However, the charge transfer during each particle-particle contact is stochastic. Therefore, while larger particles tend to acquire a net positive charge on average, individual particles may locally and temporally reverse the trend. This reversal is evident in Fig. 12c, where, up to $t = 3$ s, the charge distributions of small PS particles extend into the positive domain, and the distributions of large PS particles extend into the negative domain.

If the reference impact reveals another charging type, such as A2, B2, or C2, then the small particles would charge positively and the large ones negatively instead. Hence, we do not impose any assumptions on the charge carrier properties that would predetermine the polarity. The particle polarity emerges from the statistical parameters of the reference impact.

Interestingly, the saturation charge of the particles depends not only on their size but, in contrast to the simulations shown in Fig. 9a, also on the particle material. Here, the saturation of particle charge is not governed by the charge transfer from the wall to the particle and

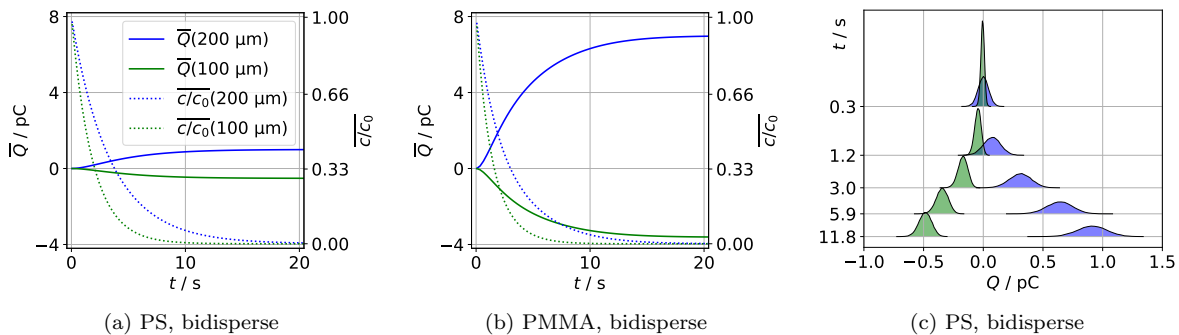


FIG. 12. Size-dependent bipolar charging of bidisperse (a) PS and (b) PMMA particles, as observed in experiments (cf. Fig. 1d). (c) Charge distributions of PS particles, separated by size: 100 μm (green) and 200 μm (blue). These simulations consider particle-particle charging in a periodical box without fluid forces.

the associated decline of α_w/α_0 . Instead, in the periodical box simulations (Fig. 12), charging terminates when all charging sites on all particles are depleted. Because the particles follow random collision histories and thus accumulate charge at different rates, the final charge is not uniform across particles (as in Figs. 9b and 9c) but follows a distribution. The final charge distribution for PS particles at $t = 11.8$ s is shown in Fig. 12c.

To summarize the CFD simulations, the SPC model successfully predicts the three particle charging patterns highlighted in the Introduction: *variable impact charge*, *charge reversal*, and *size-dependent bipolar charging*, all of which are observed in experiments. These behaviors are not the result of manual tuning or selective parameter choices. They arise naturally from the model, based solely on the scaling laws and the statistical parameters obtained from the reference impact.

IV. DISCUSSION

In this section, we discuss the accuracy and physical foundations of the SPC model.

A. Physical assumptions of the SPC model

Compared to other existing particle charging models, the SPC model, in particular Eqs. (9a) to (9d) and (12), relies on few assumptions about the physics of charge transfer, which are listed and discussed in the following.

A central assumption (Fig. 2) is that the impact charge between two surfaces can be separated into two charge transfers in opposite directions: a deterministic transfer from a conductor and a stochastic transfer from an insulator. The experiments of Matsuyama *et al.* [17] support this assumption. They showed that the impact charge of a conductive particle on a conductive target varies very little, whereas the impact charge from an insulative particle exhibits strong variability.

The current formulation models a single stochastic process on the surface of insulators: the depletion of charging sites, which is equivalent to the depletion of transferable charge carriers. One could imagine multiple overlapping stochastic processes, such as layers of different charging sites with distinct statistical parameters. Such processes could be included by introducing additional statistical parameter sets and scaling laws. However, linking the combined statistics of multiple concurrent stochastic processes to a single reference impact would be challenging. Likewise, nanoscale morphological changes due to repeated impacts that alter the impact statistics [44] would require a new conceptual framework.

The model further assumes that c_0 , ϵ_w , and ϵ_p are constant for a given material. This assumption aligns with the findings of Grosjean and Waitukaitis [32], who observed that the ratio between the correlation length of mosaic features and the donor/acceptor site size remains approximately constant across a material system. Nonetheless, this assumption necessitates a dedicated reference impact experiment for each powder under investigation, since even nominally identical powders may differ due to specific manufacturing, handling, or storage conditions.

As stated above, these physical assumptions are few compared to other charging models. Thus, the SPC model serves as a flexible mathematical framework that can, via the input parameters μ_0 , σ_0 , γ_0 , and $\Delta Q_{0,\min}$, predict a wide range of particle charging patterns.

As a stochastic model, the SPC model does not aim to predict the charge evolution of individual particles but rather the evolution of the charge distributions of the entire powder. Accordingly, it does not attempt to resolve mechanisms that depend on the history of individual particles [14] but captures powder-wide charge distributions resulting from such mechanisms' aggregation. We use a different particle in each of the $M \geq 100$ reference impact experiments per powder to capture these global effects.

This statistical treatment is consistent with the turbulence and particle dynamics modeling in Section III,

which is also meaningful only in a statistical sense. In other words, a hypothetical model that predicts the charge evolution of every individual particle would not improve the overall theoretical framework's predictive capability.

The detailed modeling of the individual terms on the right hand side of Eq. (12) is not unique to the SPC model but borrowed from contact mechanics and other disciplines. Therefore, we do not discuss their physical assumptions here. It is worth emphasizing, however, that the SPC model expresses these terms as ratios rather than absolute values. For instance, the absolute values of the charging site densities c and c_0 are not experimentally accessible and must typically be estimated. In contrast, the ratio c/c_0 is much easier to model, particularly since $c/c_0 = 1$ initially by definition, even though c is unknown.

Similarly, modeling contact areas via a Hertzian approach involves several physical assumptions that are clearly violated for real particles. Surface roughness, for example, can reduce the effective contact area by several orders of magnitude compared to the Hertzian prediction [34]. However, in the ratios A/A_0 (Eqs. (14) and (17)), many of these assumptions, including all material parameters, cancel out. Since surface roughness affects both A and A_0 equally, the relative error in their ratio is substantially smaller than the error in their absolute values.

Therefore, using ratios instead of absolute values is powerful and significantly reduces the uncertainties associated with the terms in Eq. (12).

B. Error analysis

In Section II G, we evaluated the statistical uncertainty of the SPC model's four input parameters, μ_0 , σ_0 , γ_0 , and $\Delta Q_{0,\min}$, along with the associated error introduced through scaling from one impact to another. These uncertainties typically ranged between 10% and 30%.

To assess the effect of these uncertainties on model predictions, Fig. 13 illustrates the resulting variations in particle charge distributions caused by deliberate changes to the input parameters. For this analysis, we employed the same cubical box setup without fluid forces as in simulations 5 and 6, but with wall boundary conditions instead of periodic ones (simulations 7–13; cf. Table II).

We first simulated the charging of PMMA particles using the nominal reference impact parameters listed in Table I. Then, we systematically varied each input parameter independently by +20% and -20% to quantify its influence. This uniform variation allows for a direct comparison of parameter sensitivity.

For the evolution of the average particle charge (Fig. 13a), variations in $\Delta Q_{0,\min}$ had the largest effect, while changes in μ_0 , σ_0 , and γ_0 had only minor influence. Similarly, for the particle charge distribution at $t = 0.1$ s (Fig. 13b), $\Delta Q_{0,\min}$ again showed the strongest impact,

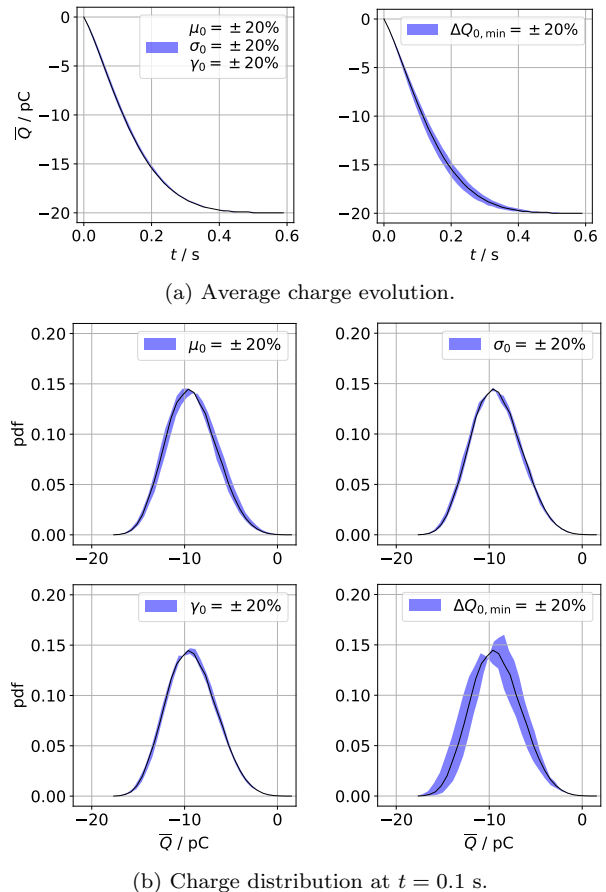


FIG. 13. The black curves show (a) the evolution of the average charge and (b) the charge distribution at $t = 0.1$ s of 200 μm sized PMMA particles. The blue shaded areas envelop their variations resulting from a $\pm 20\%$ change in one of the four SPC model input parameters. The simulations include particle-particle and particle-wall charging in a cubical box without fluid forces.

followed by μ_0 . In contrast, variations in σ_0 and γ_0 led to only modest changes in the distribution.

In summary, the model is relatively insensitive to uncertainties in σ_0 . While μ_0 strongly influences the results, it is also the most accurately determined parameter from the reference impact experiments (see Section II G). Conversely, γ_0 is the least precisely determined input, but its influence on model output is minimal.

The parameter $\Delta Q_{0,\min}$ poses particular challenges. A source of uncertainty is the classification of the impact type, i.e., whether it falls into Type A1, B1, or C1, or alternatively A2, B2, or C2 (cf. Fig. 3). Assuming that the transferable charge carriers on conductors are electrons favors Types A1 and B2; however, the possibility of Type A2 cannot be entirely ruled out.

Further, unlike the other statistical parameters, $\Delta Q_{0,\min}$ does not emerge from a converging distribution but is instead linked to a single extremal event in the experimental dataset. Although the convergence curve

shown in Fig. 6 suggests that $\Delta Q_{0,\min}$ can be estimated with relatively few experiments, we overall consider it the least reliable component of the SPC model.

C. Relation to other models

The variations of the statistical parameters plotted in Figs. 7c and 7d result in the SPC model to predict a large range of possible impact outcomes. The popular condenser model, discussed in the Introduction, is a special case of the SPC. More specifically, the SPC recovers the condenser model for $c/c_0 = 0$, which means the charge transfer is deterministic, and $\Delta Q_{0,\min} = -CU$, where C is the electric capacity and U the contact potential difference between the particle and the wall.

Also, the surface state model is a special case of the SPC model. The SPC model recovers the surface state model by switching off particle-wall impact charging and setting the SPC model parameters $\Delta Q_{0,\min}$ and σ_0 to zero. Then, the charge transfer between particles becomes deterministic.

Thus, the SPC model is a unified model that can predict same- and different-material particle charging. Existing particle-scale models are special cases of the SPC model, which specific input parameters can recover.

Since the presented SPC model builds on the mosaic model of Grosjean and Waitukaitis [32], the particle-scale quantities of the SPC model can be traced back to many of the nanoscopic quantities of the mosaic model: The contact area of the SPC model, A , is the square of the side length, L^2 , of the mosaic model's quadratic surface. The charge of one charging site, ϵ_p and ϵ_w , correlates in the mosaic model to $e(l/l_0)^2$, where l_0 is the size of one site that can transfer an elementary charge e , and l is the correlation length between charging sites. The charging site density in the SPC model, c , is $1/l^2$ in the mosaic model.

The SPC concept of charging sites that are active and charging sites that are inactive (i.e., α , green and brown spots in Fig. 2b) is similar to the donor probability p in the mosaic model. The surface density of active charging sites, αc , relates to p/l^2 in the mosaic model. The probability of an active charging site to transfer charge, p in the SPC model, is denoted by α in the mosaic model.

Further, the mosaic model predicts average- or variance-driven charging regimes, depending on whether the probability of donors on both contacting surfaces is different or equal. The SPC model recovers the same behavior for $\mu_0 = 0$, where the charge exchange is variance-driven, and for $\mu_0 \neq 0$, where the charge exchange is average-driven.

A difference between both models is that the mosaic model tracks the availability of donors and acceptors on both contacting surfaces. The SPC model tracks charging sites, which have a similar concept as donors, but assumes an acceptor probability of unity, which is one assumption underlying the surface state model. Compared

to the mosaic model, the SPC model applies a generic idea of charging sites without the need to define their physical size or geometry. Neither does the SPC model require an assumption on the type of charge carrier; it can describe both electron and ion transfer.

An important difference between the models is that the mosaic model relies on nanoscopic quantities that are difficult to access experimentally. All inputs to the SPC model are parameters on the particle scale, do not need to resolve the particle surface, and can be measured by one experimental apparatus.

The pure statistical charging model, discussed in the Introduction, differs from the SPC model in the amount of conditions that need to be measured experimentally. The statistical model requires measuring the effect of all relevant impact parameters, their variations, and cross-correlations. Given the large number of impact parameters that affect a particle's impact charge, a purely statistical model requires an exuberant number of experiments to quantify the complete parameter space. In contrast, the SPC model requires measuring exactly one reference impact condition and scales the resulting parameters to other conditions.

While the statistical model requires parameter variations, the input parameters to the SPC model become more accurate when the single reference condition is met in each particle impact experiment. Therefore, we control the initial and boundary conditions of the particle impact experiments to a high degree (see Section II G).

The essence of the SPC model lies in the scaling laws derived in Section II B. Even though we decided in Sections II C to II F on specific formulations to estimate the active charging site ratios of Eq. (12), these specific formulations are not inherent to the model. They can be exchanged for any other expressions, for example, to include more accurate contact mechanics, other contact modes, or any other parameter.

In the above formulation of the SPC model, we consider the effects of impact velocity, particle size, and initial charge on the impact charge distributions. However, by applying appropriate correlations to the ratios N_w/N_0 and N_i/N_0 , the model can be straightforwardly extended to include other contact modes, impact angles, particle shapes, surface roughness, temperature, humidity, or pressure.

V. CONCLUSIONS

We have presented the stochastic particle charging (SPC) model, a unified framework that can predict charging between the same and different materials. This unification addresses a long-standing challenge in contact electrification modeling, allowing consistent description of charge transfer between insulative particles, conductive walls, and particles in between. The model's equation system is closed by statistical parameters obtained from a single reference impact experiment. Through a set

of physically motivated laws, the model scales these parameters to a wide range of particle contacts, eliminating the need for nanoscopic surface resolution.

In our large-scale simulations of wall-bounded turbulent flows involving 300 000 insulating particles undergoing millions of collisions with each other and the conductive walls, the SPC model accounted for less than 0.01% of the total simulation time. The model reproduces three cornerstone experimental observations of triboelectric charging: Variable impact charge even for identical impact conditions, charge reversal, and size-dependent bipolar charging. By bridging nanoscale physics and system-scale simulations with minimal experimental input, the SPC model offers a shift from surface-resolved or empirical models to a versatile statistical framework.

In the future, the model would be further improved by closing the equation system without $\Delta Q_{0,\min}$, the largest source of uncertainty. The SPC model's concept predestines it for including additional physical effects such as different contact modes, particle shape, surface roughness, temperature, humidity, and pressure. As a computationally efficient and physically grounded tool, the model enables the simulation of charged particle dynamics across many scientific and engineering disciplines, including volcanic plume electrification, dust storms, pharmaceutical powder processing, and industrial process safety.

Appendix A: Scaling of $Q_{i,\max}$

During an impact on another surface, the charge transfer from particle i reaches its maximum if all active charging sites simultaneously transfer charge, which is according to Eq. (3b)

$$Q_{i,\max} = N_i \epsilon_p = \frac{\mu_i}{p}. \quad (\text{A1})$$

The unknown p can be derived from Eqs. (3b) to (3d). Combining Eqs. (3c) and (3d) leads to

$$\gamma_i = \frac{\epsilon_p(1-2p)}{\sigma_i}, \quad (\text{A2})$$

and combining Eqs. (3b) and (3c) leads to

$$\epsilon_p = \frac{\sigma_i^2}{\mu_i(1-p)}. \quad (\text{A3})$$

Then, substituting Eq. (A3) into Eq. (A2) yields

$$\gamma_i = \frac{\sigma_i(1-2p)}{\mu_i(1-p)}. \quad (\text{A4})$$

Solving this equation for p , and substituting into Eq. (A1) results in the closed expression for $Q_{i,\max}$,

$$Q_{i,\max} = \frac{\mu_i(\gamma_i \mu_i - 2\sigma_i)}{\gamma_i \mu_i - \sigma_i}, \quad (\text{A5})$$

which is the upper bound to the skew normal distribution in Eq. (10).

Appendix B: Mathematical model and simulation set up

We implemented the SPC model (Section II) in the open source CFD tool pafix [38], which employs a coupled Eulerian-Lagrangian approach. It solves the Navier-Stokes equations for the carrier gas flow in Eulerian framework and tracks each particle individually in Lagrangian framework. The resulting fluid velocity profiles, particle concentration profiles and the particles' response to the electric field have been extensively validated and documented [39, 45, 46] in the last years.

The Navier-Stokes equations for constant densities and diffusivities read

$$\nabla \cdot \mathbf{u}_f = 0 \quad (\text{B1a})$$

$$\frac{\partial \mathbf{u}_f}{\partial t} + (\mathbf{u}_f \cdot \nabla) \mathbf{u}_f = -\frac{1}{\rho_f} \nabla p_f + \nu_f \nabla^2 \mathbf{u}_f + \mathbf{f}_f. \quad (\text{B1b})$$

Therein, \mathbf{u}_f is the fluid velocity, ρ_f the density, p_f the dynamic pressure, and ν_f the kinematic viscosity.

For the simulations presented in Section III, we model a section of the duct, apply periodic boundary conditions in the streamwise direction, and drive the flow by the pressure gradient, \mathbf{f}_f . In the above equations, second-order schemes approximate the spatial and temporal derivatives.

The computational domain resembles a square-shaped duct with a side length of 5 cm and a streamwise length of 24 cm. Based on the duct's side length, the flow's bulk Reynolds number is approximately 5400, and its frictional Reynolds number is 360. The domain is discretized by $256 \times 144 \times 144$ grid points, and turbulence is resolved via direct numerical simulation (DNS).

For each particle of mass m , we solve the acceleration, \mathbf{a} , based on Newton's second law of motion,

$$m\mathbf{a} = \mathbf{F}_d + \mathbf{F}_l + \mathbf{F}_c + \mathbf{F}_e + \mathbf{F}_g. \quad (\text{B2})$$

The drag force acting on the particle, \mathbf{F}_d , is computed using the empirical correlation of Putnam [47]. The lift force, \mathbf{F}_l , incorporates the formulation of Saffman [48] and its correction by Mei [49] to account for particle Reynolds numbers exceeding the shear Reynolds number. The collisional force, \mathbf{F}_c , includes both particle-particle and wall-particle interactions. To detect particle-particle collisions, we implemented ray casting [50, 51], a variant of the hard-sphere collision model.

Electrostatic forces, \mathbf{F}_e , acting on a particle carrying charge Q , are computed using a hybrid method [39]. This approach combines near-field Coulomb interactions between a particle and its neighbors with far-field forces calculated via Gauss's law. The final term in Eq. (B2), $\mathbf{F}_g = m\mathbf{g}$ with $\mathbf{g} = (9.81, 0, 0)^T \text{ms}^{-2}$, denotes the gravitational force, indicating that we simulate a downward flow.

Equation (B2) is numerically integrated using a second-order Crank-Nicolson scheme.

TABLE II. Parameters of all CFD simulations.

	Material	r (μm)	ρ_p (kg/m^3)	pnd ($\#/\text{m}^3$)	Flow type	Charging models	Figs.
1	PS	200	1000	5.0×10^8	wall-bounded turbulence	particle-wall & particle-particle	8, 9(a), 9(b), 10
2	PMMA	200	1150	5.0×10^8	wall-bounded turbulence	particle-wall & particle-particle	9(a), 9(c), 14
3	PS	100	1000	5.0×10^8	wall-bounded turbulence	particle-wall	11(a)
4	PMMA	100	1150	5.0×10^8	wall-bounded turbulence	particle-wall	11(b)
5	PS	200	1000	2.5×10^8	periodical box, no fluid	particle-particle	12(a), 12(c)
		100	1000	2.5×10^8			
6	PMMA	200	1150	2.5×10^8	periodical box, no fluid	particle-particle	12(b)
		100	1150	2.5×10^8			
7–13	PMMA	200	1000	5.0×10^8	cubical box, no fluid	particle-wall & particle-particle	13

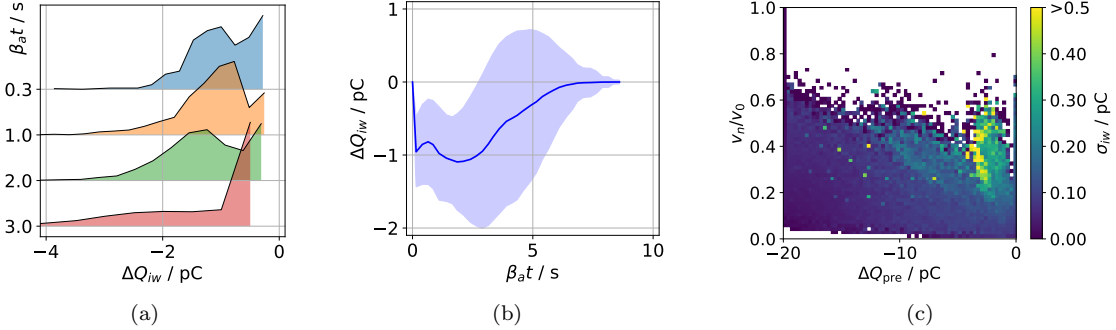


FIG. 14. Variable impact charge for 200 μm sized PMMA particles, predicted by the SPC model, analogous to the impact charge of the PS particles (cf. Fig. 10) (a) Charge distributions for selected time instances. (b) Variation of the impact charge and its standard deviation with time. (c) Variation of the impact charge for identical impact velocity and initial charge.

All simulations' parameters are summarized in Table II.

Appendix C: Variable impact charge PMMA

For completeness, Fig. 14 presents the variable impact charge of PMMA particles, analogous to Fig. 10 for PS. Figures 10 and 14 show qualitatively similar behavior.

However, a comparison between the figures reveals that the statistical parameters of the charge distributions depend not only on the contact type and temporal evolution but also strongly on the particle material. The observed temporal change arises from the evolving particle properties, such as the average increase in particle charge and the depletion of charging sites on the particle surfaces (Fig. 9). These evolving properties influence the statistical parameters through the ratio N_i/N_0 (cf. Eq. (12)).

Overall, PMMA particles exhibit higher impact charges compared to PS. Consequently, PMMA particles accumulate charge more rapidly. As α_w/α_0 increases quickly, the charge transfer becomes self-limiting already after 7 s.

Appendix D: Nomenclature of the SPC model

A	contact area (m^2)	χ_p	elasticity parameter particle ($\text{m}^2 \text{N}^{-1}$)
A_0	A for reference impact (m^2)	χ_w	elasticity parameter wall ($\text{m}^2 \text{N}^{-1}$)
A_p	particle surface area (m^2)	ϵ_p	charge of one particle charging site (C)
A_w	A between particle and wall (m^2)	ϵ_w	charge of one wall charging site (C)
A_{ij}	A between two particles (m^2)	γ_0	skewness of ΔQ_{iw} for reference impact
C_{sat}	fitting parameter for Eq. (22) (C m^{-2})	γ_i	skewness of Q_i
E	electric field strength at particle surface (V m^{-1})	γ_{i0}	skewness of Q_i for reference impact (C)
E_{sat}	saturation of E (V m^{-1})	μ_0	mean of ΔQ_{iw} for reference impact (C)
E_i	E at particle-wall contact (V m^{-1})	μ_i	mean of Q_i (C)
E_{ij}	E at particle-particle contact (V m^{-1})	μ_w	mean of Q_w (C)
M	number of reference impact or impacts	μ_{i0}	mean of Q_i for reference impact (C)
N	number of active charging sites	μ_{w0}	mean of Q_w for reference impact (C)
N_0	N at contact area of particle for reference impact	ρ_p	particle density (kg m^{-3})
N_i	N at contact area of particle	σ_0	standard deviation of ΔQ_{iw} for reference impact (C)
N_w	N at contact area of wall	σ_i	standard deviation of Q_i
N_{w0}	N at contact area of wall for reference impact	σ_{i0}	standard deviation of Q_i for reference impact (C)
Q	particle charge (C)	ε	electric permittivity of gas phase ($\text{C V}^{-1} \text{m}^{-1}$)
Q_{pre}	Q before impact (C)	c	surface density of charging sites (m^{-2})
Q_{sat}	saturation of Q (C)	c_0	c for reference impact (m^{-2})
Q_i	charge transfer of particle i to other surface (C)	k_e	restitution coefficient
Q_w	charge transfer from wall to particle (C)	p	probability that active site transfers charge
$Q_{i,\text{max}}$	maximum Q_i to other surface (C)	r	particle radius (m)
ΔQ	impact charge (C)	r_0	r in reference impact (m)
$\Delta Q_{0,\text{min}}$	minimum ΔQ of reference impact	v_0	v_n for reference impact (m s^{-1})
ΔQ_{ij}	ΔQ of particle i after contact with particle j (C)	v_n	normal impact velocity of particle on wall (m s^{-1})
ΔQ_{iw}	ΔQ of particle i after wall contact (C)	v_{ij}	relative impact velocity of two particles (m s^{-1})
α	ratio of active to total number of charging sites		
α_0	α for reference impact		
α_i	α for particle to wall transfer		
α_w	α for wall to particle transfer		
α_{ij}	α for particle to particle transfer		
β_a	artificial increase of A		
β_c	increase of A due to contact mode		
β_r	increase of A due to surface roughness		

ACKNOWLEDGMENTS

This project has received funding from the European Research Council (ERC) under the European Union's Horizon 2020 research and innovation programme (grant agreement No. 947606 PowFEct).

-
- [1] C. Cimorelli and K. Genareau, A review of volcanic electrification of the atmosphere and volcanic lightning, *J. Volcanol. Geotherm. Res.* **422**, 107449 (2022).
- [2] A. K. Kamra, Physical sciences: Visual observation of electric sparks on gypsum dunes, *Nature* **240**, 143 (1972).
- [3] T. Shinbrot, K. LaMarche, and B. J. Glasser, Triboelectrification and razorbacks: Geophysical patterns produced in dry grains, *Phys. Rev. Lett.* **96**, 178002 (2006).
- [4] J. Méndez Harper, C. S. McDonald, E. J. Rheingold, L. C. Wehn, R. E. Bumbaugh, E. J. Cope, L. E. Lindberg, J. Pham, Y.-H. Kim, J. Dufek, and C. H. Hendon, Moisture-controlled triboelectrification during coffee grinding, *Matter* **7**, 266 (2024).
- [5] A. Giffin and P. Mehrani, Effect of gas relative humidity on reactor wall fouling generated due to bed electrification in gas-solid fluidized beds, *Powder Technol.* **235**, 368 (2013).
- [6] A. Oshawa, Statistical analysis of fires and explosions attributed to static electricity over the last 50 years in Japanese industry, *J. Phys.: Conf. Ser.* **301**, 012033 (2011).
- [7] A. Grayver, Unravelling the electrical conductivity of earth and planets, *Surv. Geophys.* **45**, 187 (2024).
- [8] J. M. Zernhelt, M. Mor, and D. S. Juda, Coffee grinder with static electricity ground, Patent reference: US10912418 (2021), <https://patents.justia.com/patent/10912418>.
- [9] IEC 60079-32-1, *Explosive Atmospheres – Part 32-1: Electrostatic Hazards*, Technical Specification (2012).
- [10] H. Grosshans, W. Xu, and T. Matsuyama, Simulation of PMMA powder flow electrification using a new charging model based on single-particle experiments, *Chem. Eng. Sci.* **254**, 117623 (2021).
- [11] S. L. Soo, Dynamics of charged suspensions, in *Topics in Current Aerosol Research* (Pergamon Press, 1971) pp. 71–73.
- [12] H. Masuda, T. Komatsu, and K. Inoya, The static electrification of particles in gas-solids pipe flow, *AIChE J.* **22**, 558 (1976).
- [13] W. John, G. Reischl, and W. Devor, Charge transfer to metal surfaces from bouncing aerosol particles, *J. Aerosol Sci.* **11**, 115 (1980).

- [14] G. Grosjean and S. Waitukaitis, Single-collision statistics reveal a global mechanism driven by sample history for contact electrification in granular media, *Phys. Rev. Lett.* **130**, 098202 (2023).
- [15] P. E. Shaw, C. S. Jex, and W. B. Hardy, Tribo-electricity and friction. II.—Glass and solid elements, *Proc. R. Soc. A* **118**, 10.1098/rspa.1928.0037 (1928).
- [16] K. M. Forward, D. J. Lacks, and R. M. Sankaran, Charge segregation depends on particle size in triboelectrically charged granular materials, *Phys. Rev. Lett.* **102**, 028001 (2009).
- [17] T. Matsuyama, M. Ogu, H. Yamamoto, J. C. M. Marijnissen, and B. Scarlett, Impact charging experiments with single particles of hundred micrometre size, *Powder Technol.* **135–136**, 14 (2003).
- [18] T. Matsuyama and H. Yamamoto, Impact charging of particulate materials, *Chem. Eng. Sci.* **61**, 2230 (2006).
- [19] J. Lowell and I. Truscott, Triboelectrification of identical insulators. II. Theory and further experiments, *J. Phys. D: Appl. Phys.* **19**, 1281 (1986).
- [20] S. R. Waitukaitis, V. Lee, J. M. Pierson, S. L. Forman, and H. M. Jaeger, Size-dependent same-material tribocharging in insulating grains, *Phys. Rev. Lett.* **112**, 218001 (2014).
- [21] H. T. Baytekin, B. Baytekin, J. T. Incorvati, and B. A. Grzybowski, Material transfer and polarity reversal in contact charging, *Angew. Chemie Int. Ed.* **51**, 4843 (2012).
- [22] D. J. Lacks, N. Duff, and S. K. Kumar, Nonequilibrium accumulation of surface species and triboelectric charging in single component particulate systems, *Phys. Rev. Lett.* **100**, 188305 (2008).
- [23] D. J. Lacks and A. Levandovsky, Effect of particle size distribution on the polarity of triboelectric charging in granular insulator systems, *J. Electrostat.* **65**, 107 (2007).
- [24] H. Grosshans and M. V. Papalexandris, A model for the non-uniform contact charging of particles, *Powder Technol.* **305**, 518 (2016).
- [25] X. Liu, J. Kolehmainen, I. Nwogbaga, A. Ozel, and S. Sundaresan, Effect of particle size on tribocharging, *Powder Technol.* **375**, 199 (2020).
- [26] J. Lowell and I. Truscott, Triboelectrification of identical insulators. I. An experimental investigation, *J. Phys. D: Appl. Phys.* **19**, 1273 (1986).
- [27] S. Jantač and H. Grosshans, Suppression and control of bipolar powder charging by turbulence, *Phys. Rev. Lett.* **132**, 054004 (2024).
- [28] M. Apodaca, P. Wesson, K. Bishop, M. Ratner, and B. Grzybowski, Contact electrification between identical materials, *Angew. Chem. Int. Ed.* **49**, 946 (2019).
- [29] H. T. Baytekin, M. Patashinski, A. Z. Branicki, B. Baytekin, S. Soh, and B. A. Grzybowski, The mosaic of surface charge in contact electrification, *Science* **33**, 308 (2011).
- [30] B. D. Terris, J. E. Stern, D. Rugar, and H. J. Mamin, Contact electrification using force microscopy, *Phys. Rev. Lett.* **63**, 2669 (1989).
- [31] T. A. L. Burgo, T. R. D. Ducati, K. R. Francisco, K. J. Clinckspoor, F. Galembeck, and S. E. Galembeck, Triboelectricity: Macroscopic charge patterns formed by self-arranging ions on polymer surfaces, *Langmuir* **28**, 7407 (2012).
- [32] G. Grosjean and S. Waitukaitis, Asymmetries in triboelectric charging: Generalizing mosaic models to different-material samples and sliding contacts, *Phys. Rev. Mater.* **7**, 065601 (2023).
- [33] Y. Zhang, A. Ozel, and C. M. Hartzell, A macroscopic donor–acceptor-based discrete element model for contact electrification of insulating granular materials, *Powder Technol.* **431**, 119029 (2024).
- [34] S. Jantač, J. Pelcová, J. Sklenářová, M. Drápela, H. Grosshans, and J. Kosek, Triboelectric charging model for particles with rough surfaces, *Adv. Powder Technol.* **36**, 104787 (2025).
- [35] P. M. Ireland, The role of changing contact in sliding triboelectrification, *J. Phys. D: Appl. Phys.* **41**, 025305 (2008).
- [36] P. M. Ireland, Dynamic particle-surface tribocharging: The role of shape and contact mode, *J. Electrostat.* **70**, 524 (2012).
- [37] T. Matsuyama, A discussion on maximum charge held by a single particle due to gas discharge limitation, in *AIP Conference Proceedings*, Vol. 1927 (American Institute of Physics, 2018) p. 02001.
- [38] pafIX, <https://gitlab1.ptb.de/asep/pafix> (2021).
- [39] H. Grosshans and M. V. Papalexandris, On the accuracy of the numerical computation of the electrostatic forces between charged particles, *Powder Technol.* **322**, 185 (2017).
- [40] K.-H. Grote and J. Feldhusen, *Dubbel* (Springer, Wiesbaden Berlin Heidelberg, 2007).
- [41] W. Domke, *Werkstoffkunde und Werkstoffprüfung* (Cornelsen, Berlin, 1986).
- [42] N. Mujica and S. Waitukaitis, Accurate determination of the shapes of granular charge distributions, *Phys. Rev. E* **107**, 034901 (2023).
- [43] J. Haeberle, A. Schella, M. Sperl, M. Schröter, and P. Born, Double origin of stochastic granular tribocharging, *Soft Matter* **14**, 4987 (2018).
- [44] J. C. Sobarzo, F. Pertl, D. M. Balazs, T. Costanzo, M. Sauer, A. Foelske, M. Ostermann, C. M. Pichler, Y. Wang, Y. Nagata, M. Bonn, and S. Waitukaitis, Spontaneous ordering of identical materials into a triboelectric series, *Nature* **638**, 664 (2025).
- [45] G. Ozler, M. Demircioglu, and H. Grosshans, Effect of drag force modelling on the flow of electrically charged particles, *Adv. Powder Technol.* **34**, 103951 (2023).
- [46] H. Grosshans, Influence of weak electrostatic charges and secondary flows on pneumatic powder transport, *Can. J. Chem. Eng.* **101**, 2347–2360 (2022).
- [47] A. Putnam, Integratable form of droplet drag coefficient, *ARS J.* **31**, 1467 (1961).
- [48] P. G. Saffmann, The lift on a small sphere in a slow shear flow, *J. Fluid Mech.* **22**, 385 (1965).
- [49] R. Mei, An approximate expression for the shear lift on a spherical particle at finite reynolds number, *Int. J. Multiphase Flows* **18**, 145 (1992).
- [50] S. D. Roth, Ray casting for modeling solids, *Comput. Graphics Image Process.* **18**, 109 (1982).
- [51] T. Schroeder, Collision detection using ray casting, *Game Dev.* **8**, 50 (2001).